Highlights

Bayesian Optimization of a Collimated HPGe Detector Model for Segmented Gamma Scanning

Victor J. Casas-Molina, Eric Laloy, Bart Rogiers, Tom Dhaene, Ivo Couckuyt

- Characterizing the spatial response of a collimated detector is important in SGS
- We inferred relevant parameters for calibration of the SGS arrangement via BO.
- The optimization was performed considering the spatial response of the arrangement.
- The parameters and the model were validated for different collimator configurations.

Bayesian Optimization of a Collimated HPGe Detector Model for Segmented Gamma Scanning

Victor J. Casas-Molina[a,b], Eric Laloy[a], Bart Rogiers[a], Tom Dhaene[b], Ivo Couckuyt[b]

[a]*Sustainable Waste & Decommissioning, Belgian Nuclear Research Centre (SCK CEN), Boeretang 200, Mol, 2400, Belgium*
[b]*Department of Information Technology, Ghent University-imec, Technologiepark-Zwijnaarde 126, Ghent, 9052, Belgium*

Abstract

Segmented Gamma Scanning (SGS) is an important technique for quantifying gamma-emitting isotopes in radioactive waste packages. Collimated High-Purity Germanium (HPGe) detectors are commonly employed due to their superior resolution. However, calibrating HPGe detectors equipped with complex collimators poses challenges, especially regarding the modeling of the spatial response of the detector. This work introduces a calibration methodology for the Full Energy Peak Efficiency (FEPE) of HPGe detectors equipped with variable aperture collimators using Bayesian optimization to handle their complex geometries. The method and the model were then validated for the full range of application of the detector-collimator arrangement using experimental FEPE measurements, demonstrating the model's potential for accurate SGS simulations.

Keywords: HPGe Detector, Segmented Gamma Scanning, Bayesian Optimization, Collimator, Dead Layer, PHITS

1. Introduction

Segmented Gamma Scanning (SGS) is a non-destructive technique for inspecting radioactive waste packages, using gamma spectrometry to identify and quantify gamma-emitting isotopes. Semiconductor detectors like

Email address: victor.casas.molina@sckcen.be (Victor J. Casas-Molina)

High-Purity Germanium (HPGe) are preferred for SGS due to their superior resolution and wide detection range.

HPGe detectors can resolve small photopeaks across the full gamma spectrum relevant for waste characterization. SGS involves scanning the package in horizontal segments, with the HPGe detector equipped with a collimator to reduce crosstalk and ensure proper spatial separation of segments.

However, HPGe detectors require initial and periodic calibration due to efficiency loss over time. Calibration often uses computational Monte Carlo (MC) models to determine uncertain detector parameters affecting intrinsic efficiency. This by employing methods like direct search, sequential optimization, analytic approximation, or response surface methodology [1, 2, 3, 4].

Although numerous calibration methods have been proposed for various detectors, to the best of our knowledge, no method suited to SGS detectors with complex collimators exists to date. The spatial response of the detector is essential in SGS calibration. However, SGS collimators can be geometrically complex [5], especially when they have a variable aperture, while accounting for the detector's spatial response in the calibration is essential. Altogether this makes the calibration of collimated SGS detectors challenging.

Because of the sensitivity of the detector's efficiency to the relative positions of the source, detector and collimator, for collimated detectors it is crucial to spatially characterize the detector-collimator arrangement with multiple sources or distributed sources rather than single point source measurements. Furthermore, this behavior of collimated detectors leads to a somewhat high-dimensional parameter space to search in the calibration process, which may become computationally prohibitive for traditional calibration methods.

Bayesian optimization (BO) is a powerful, gradient-free tool for expensive black-box optimization problems [6]. BO uses a probabilistic model, typically a Gaussian process (GP) [7], to emulate the mean and uncertainty of the objective function to minimize (or maximize). An acquisition function then guides the selection of the next query point, balancing exploration and exploitation of the searched parameter space. BO iteratively (i) selects points to evaluate, and (ii) updates the GP, until a stopping criterion is met [8].

This process allows BO to focus on promising regions of the parameter space. By using a surrogate model to guide the search, BO is particularly suited to problems with a small objective function evaluation budget [9].

This paper introduces a new HPGe detector calibration methodology for SGS that relies on BO to deal with complex geometries with respect to both the detector itself and the associated collimator. Using a set of Full Energy Peak Efficiency (FEPE) measurements with a known point source, our approach is shwon to be able to determine the effective geometrical parameters of both components.

The remainder of this paper is organized as follows. Section 2, describes the experimental setup and the optimization methodology. This is followed by section 3 that presents the results of the optimization. Section 4 then provides some discussion of our approach before a conclusion is given in section 5.

2. Materials and methods

We consider a specific measurement system: SYSCADE. A mobile laboratory designed for the inspection and characterization of nuclear waste [10]. The SYSCADE system employs a HPGe detector equipped with a flexible collimator that can shut its lateral slabs to adjust the angular aperture as needed.

2.1. Detection system

The detector is a P-type Coaxial HPGe detector, model GCD 50210, produced by Baltic Scientific Instruments (BSI). This detector is electrically cooled and presents a Ge crystal with dimensions of ∅70 x 53.2 mm. The efficiency response was characterized by using two point sources with identical geometry: ^{241}Am with a gamma emission of 59.54 keV, and ^{152}Eu, for which seven different peaks could be measured at 121.78, 244.70, 344.28, 778.91, 964.08, 1112.08 and 1408.01 keV.

It offers a maximum resolution of 1152 eV for 122 KeV and 1854 eV for 1332 KeV, along with a relative efficiency of no less than 50.6 measured with respect to a (NaI)TI detector. The approximate internal dimensions of the detector are illustrated in Fig. 1a. As a measure of verification an X-Ray scan was taken (see Fig. 1b) which revealed that there are no substantial discrepancies in the crystal dimensions. However, a noticeable difference is apparent between the nominal crystal-to-endcap distance and the measured one.

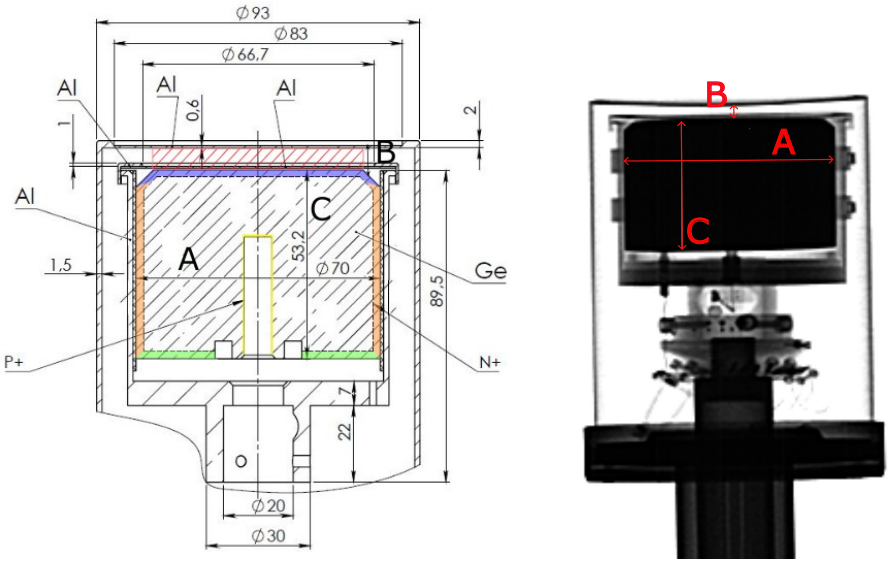

(a) Detector layout.

(b) X-ray image of the detector.

Figure 1: Detector setup. Panel (a) depicts the nominal internal dimensions of the detector. he purple, orange, green and yellow-colored areas correspond to the frontal, lateral, back and inner dead layers, respectively. The dashed red lines denote the area between crystal and endcap. Panel (b) shows the X-ray image of the detector. Measured dimensions were: A (crystal diameter), 70.05 mm, B (distance to endcap), 5.88 mm and C (crystal depth), 53.16 mm.

In the setup, the detector is housed within a lead box (Fig. 2a). The side of the box facing the detection zone measures 100 x 190 mm. The box is centrally positioned within a cylindrical cavity of 103.90 mm diameter. There is an offset of 12 mm from the box surface to the exterior surface of the detector endcap.

The detector can be displaced along two axes: vertically, allowing movement up and down, and in depth, closer to or farther away from the radiation source with an uncertainty in the displacement that is never larger than one millimeter according to the detector manufacturer.

The collimator used in this setup is made of lead and has a thickness of 80 mm (Fig. 2b). It consists of two movable lateral parts and two fixed parts at the top and bottom. The lateral parts can be adjusted horizontally to

accommodate different activity levels and dimensions of the objects placed in front of it for scanning. The external frame is made of Aluminum.

When the collimator is fully closed, its profile aligns with that of the box. The horizontal aperture of the collimator can vary from 10 mm to 60 mm, and the lateral wedges are set at a nominal angle of 10 degrees. The vertical dimension of the collimator window is fixed at 60 mm. The collimator is fixed to the box by using three M8 bolts.

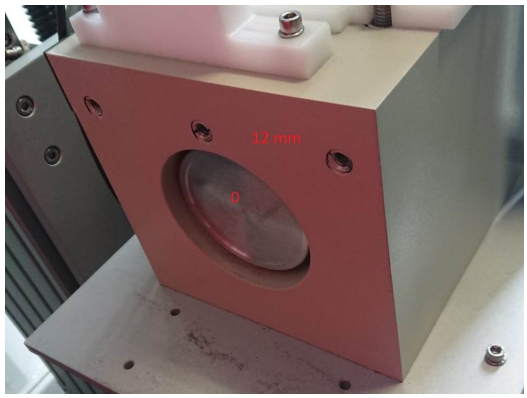

(a) Detector without collimator.

(b) Detector with the collimator assembled.

Figure 2: Detector setup. In the panel (a) the origin of coordinates of the system of reference used is marked with '0', please note the offset between the detector and the lead box. Panel (b) shows the collimator once assembled with a 60 mm aperture measured on the detector side.

2.2. Parameter selection for optimization

We present the most relevant parameters to be determined in order to calibrate the efficiency. These parameters are chosen by relevance on their

impact on the intrinsic efficiency according to the literature and eventually, the physical phenomena underlying the detection.

It is known that the Dead Layer (DL) thickness increases with time because of the diffusion of the dopants, especially if the detector is not kept at very low temperature. It is also well documented that the dead layer thickness plays a crucial role in the detector efficiency deterioration [11, 12]. The effect of the dead layer thickness is two-faced: firstly, because of the partial energy depositions by photons in the dead layer region, secondly, increasing the volume of the dead layers implies a decreasing of the active volume of the crystal thereby reducing the probability of interaction of the photons.

The germanium crystal, encased in a vacuum within a primary casing, is then placed in a secondary casing to protect it from mechanical damage. A thinner section at the front of this secondary casing, known as the detector window, improves measurement capabilities.

During calibration, it is essential to determine the distance from the detector window to the crystal's frontal surface and the thickness of the window itself. These measurements play a crucial role in understanding the detector's behavior [13, 14].

Nonetheless, for the energy range studied in this work (60 keV to 1400 keV), the change of certain parameters do not have a very strong effect over the FEPE, such is the case of the back dead layer, that according to the literature, exhibits a strong influence on the FEPE only at energies greater than 1.5 MeV [15].

On the other hand, and according to [16], the endcap thickness is normally negligible, it is made of aluminium which has a low atomic number, while the endcap thickness is too small to significantly influence the efficiency.

Therefore, among all the detector internal parameters, only the Frontal, Lateral and Inner regions of the dead layer were chosen, as well as the distance between the crystal frontal surface and the endcap. Additionally, the relative position of the detector axis with respect to the lead box cavity was also taken into account by considering the offset between box and detector centers.

Table 1 lists the parameters selected for optimization.

Table 1: Parameters chosen for optimization.

Detector parameters	**Affects:**	**Bounds**	**Units**
Frontal DL	FEPE for E $<$ 400 keV [15]	[0.60, 1.60]	mm
Lateral DL	FEPE for E $>$ 300 keV [15]	[0.60, 1.60]	mm
Inner DL	FEPE, weakly [17]	[0.01, 0.02]	mm
Distance crystal-endcap	crystal positioning	[5.30, 7.00]	mm
Vertical offset Y	detector positioning	[-1.50, 1.50]	mm
Horizontal offset X	detector positioning	[-4, 4]	mm
Collimator parameters			
Horizontal aperture	aperture, centering	[59.00, 61.00]	mm
Vertical aperture	aperture, centering	[60.00, 61.00]	mm
Slab angle	actual slab geometry	[19.00, 20.40]	deg

The collimator parameters are geometry-dependent, and given the studied geometry of the considered collimator, we selected parameters that account for both the geometry of the slabs and the actual non-shadowed area, i.e., the vertical and horizontal aperture. These parameters are quite important in the case of SGS since using poor estimates of them will greatly affect the modelled efficiency when the source is located away from the detector axis.

The optimization requires bounds on the search space to avoid selection of unrealistic parameter values. These bounds were selected based on the uncertainties provided by the manufacturer when available. For the dead layer thicknesses, no information was given by the manufacturer and the bounds were thus selected based on the literature [18].

2.3. Experimental acquisitions

Table collection is divided in three sets of experiments. The first one serves as the experimental reference required to compute an error function for the optimizer, herein the calibration experimental set (CES). The second (VE1) and third (VE2) sets were validation experiments devoted to check performance of our BO-based calibrated detector model.

VE1, was performed without the collimator, such that the consistency of the derived parameters for the detector internals could be checked. VE2 consisted of repeating the calibration measurements with different collimator apertures in order to verify that the optimized collimator parameters are consistent. The two point sources of ^{241}Am and ^{152}Eu were measured for 5 minutes in each position. Table 2 describes the setup for every experiment.

Table 2: Sources and detector settings employed in the experiments. Uncertainties are presented as two times the standard deviation.

Exp.	**Source**	**Activity (KBq)**	**Collimator aperture (mm)**
CES	^{241}Am	410.88 ± 14.38	
	^{152}Eu	392.52 ± 11.78	60
VE 1	^{241}Am	410.88 ± 14.38	
	^{152}Eu	392.52 ± 11.78	–
VE 2	^{241}Am	410.88 ± 14.38	
	^{152}Eu	392.52 ± 11.78	50 and 40

For the CES, VE1 and VE2 experiments, the same source location design was used. It consisted of a 5x5 planar square-shaped grid perpendicular to the detector axis and located 20 cm away from the detector window. The center square was perfectly aligned with the center of the detector window and all the points are equispaced as shown in Fig. 3. The position of the sources was found by performing preliminary tests and was found to properly capture the attenuation effect of the collimator in both the vertical and horizontal directions.

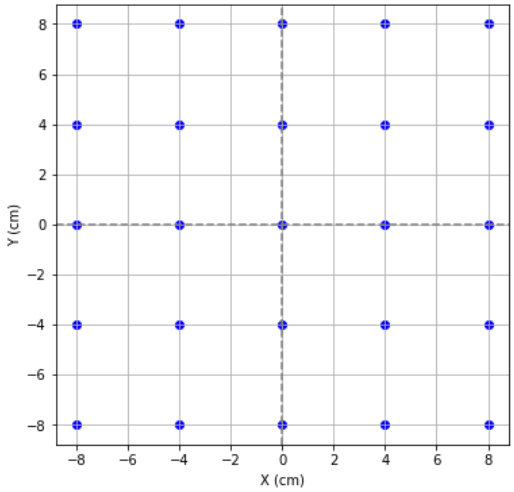

Figure 3: Positions for the sources 20 cm away from the detector window (X and Y are horizontal and vertical displacement, respectively). The center of the collimator window is aligned with (0,0).

The FEPE ($\mathcal{E}_{exp}$) was calculated for all the peaks recorded by the detector according to Eq. (1).

$$\mathcal{E}_{exp} = \left(\frac{N}{A \cdot P_\gamma \cdot t} \right) \cdot C_s \tag{1}$$

where N is the net counts for a given photopeak, A is the activity of the considered point source, P_γ the emission probability of that photopeak and t is measurement time of the detector. C_s represents a factor for the coincidence summing correction that was considered negligible (C_s=1) after its estimation using EFFTRAN [19] .

The uncertainty can be propagated to $\mathcal{E}_{exp}$ using the propagation law for uncorrelated variables, which is used for calculating the variance of the FEPE.

$$\mathrm{Var}(\mathcal{E}_{\mathrm{exp}}) = \mathcal{E}_{\mathrm{exp}}^2 \left(\frac{\mathrm{Var}(N)}{N^2} + \frac{\mathrm{Var}(A)}{A^2} + \frac{\mathrm{Var}(P_\gamma)}{P_\gamma^2} + Var(Pos) \right) \tag{2}$$

The net counts and their variance were directly given by the manufacturer software whereas the variance for P_γ was obtained from [20]. The $Var(Pos)$

variable accounts for the uncertainty of the efficiency induced by the uncertainty in the source position. The latter was estimated by perturbing the positions by 1 mm. This leads to a $Var(Pos)$ value of 9.76 %.

2.4. Monte Carlo Simulation Using PHITS Code

The MC computational model of the collimated detector was developed using the PHITS particle transport simulation code [21]. Typically, the input for a MC model includes parameters for the source, the problem environment (in this case the detection setup), the chosen tally for recording the outputs of interest, and some control parameters related to computational practicalities.

The simulation of the FEPEs was conducted using a peak-by-peak approach. This means that each run simulated and tallied only one energy peak, which simplifies post processing since background subtraction can be implemented without taking into account the effects of neighboring or overlapping peaks.

For simplicity, point sources are considered to have no thickness. The casing is also omitted, since the thickness and density of the plastic was found to be negligible during simulations, therefore, the active region was modelled as a disc of 1.5 mm of radius. For all the cases it was supposed a mono-energetic source, however, to emulate an actual detector response, the resolution of the detector was considered by inducing a Gaussian shape in the peak by employing the fitted parameters Fano (F), that accounts for best variance/mean ratio in the peak amplitude obtainable from the detector resolution, and σ_r that accounts for its resolution. According to the PHITS manual, the broadening of the Gaussian peak as a function of energy, σ_{peak}, is given by:

$$\sigma_{peak} = \sqrt{\sigma_r + FE} \tag{3}$$

Where E is energy. This is homologous to the well known expression for fitting the Full Width at Half-Maximum (FWHM) parameter. The σ_r and F parameters were obtained by fitting Eq. 3 to the experimental efficiency values measured for a ^{152}Eu point source.

It is worth noting that the PHITS default model does not transport electrons due to the computational demand associated with charged particle calculations. However, in this case, the tallying of electrons is essential as they are the particles generated by the interactions of photons within the germanium crystal. Therefore, the EGS5 model [22] integrated within the PHITS code was used to perform the simulations.

2.4.1. modeling the detector

The detector measurements for modeling the geometry were taken directly from the manufacturer (Fig. 1a). Both, the chemical composition and the density from the different components were taken from [23]. It is important to note that in the dead layers of an HPGe detector, which are the undepleted zones of the crystal, the constituent material is impure germanium, and not lithium [24]. Therefore, considering the density of these layers as that of pure germanium is a reasonable approximation.

Figure 4 presents various views of the detector model, assuming nominal parameter values. Although the figure scale makes it difficult to discern the dead layers, they are of course incorporated into the model. The region colored in white is considered to be vacuum, while the rest of the system is surrounded by air, with a density corresponding to 20 °C and 1 atm.

As one can notice, the aluminum frames and table that hold the collimator slabs have not been modelled since their contribution to the attenuation of the signal is negligible for the angle of view of the collimator. Similarly, the high voltage power supply and control unit have been omitted. The reason for this is that they are located at the back of the detector, making their impact on the signal also negligible.

2.4.2. Tallying the efficiency

The tallied region corresponds to the active volume of the crystal, which is the remaining volume after the subtraction of the dead layer volume. In this region, the tracked score is the energy deposition by the photon incidence, that generates electron-hole pairs in the active region of the crystal. The energy resolution was set to be 150 groups with a mesh divided equally in linear scale for all the simulations. These groups can be equaled to the channel concept used in current gamma spectrometry equipment.

Since the simulations are normalized to the number of history particles, the efficiency can be directly obtained by integrating under the tally and finding the net peak area.

Given that only one peak is reproduced per simulation, a simple approach for background subtraction, like the Covell method, seems sound enough for this task. The Covell method estimates the background using the counts (C) in groups of channels located at the upper and lower energy edges of the peak region [25]. Therefore the net area under the peak, i.e., the full energy peak efficiency ($\mathcal{E}_{MC}$), can be obtained by removing the background beneath the peak (B) from the gross counts (G), which amounts to sum up the contents

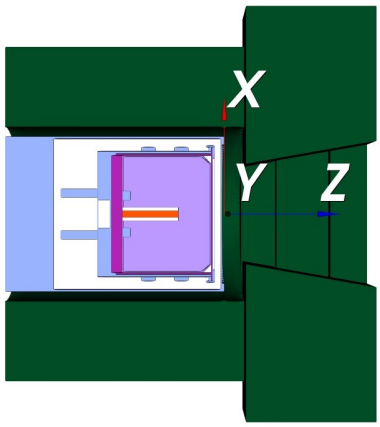

(a) Horizontal cut top view

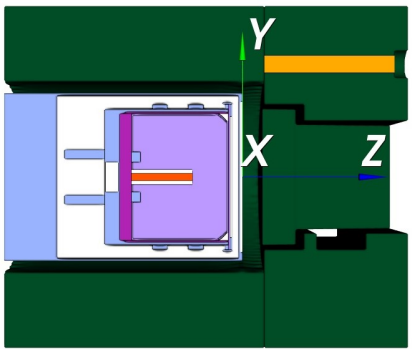

(b) Vertical cut side view

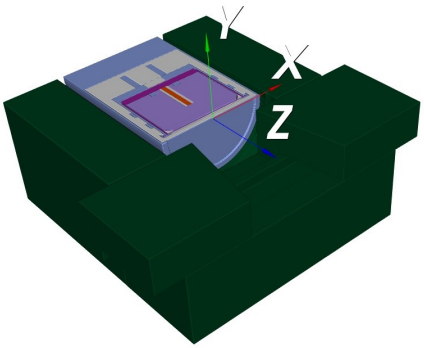

(c) 3D perspective

Figure 4: PHITS model of the detection system

in the 150 groups (n):

$$\mathcal{E}_{MC} = G - B = \sum_{i=L}^{U} C_i - \frac{n}{2m}\left(\sum_{i=L-m}^{U} C_i + \sum_{i=U+1}^{U+m} C_i\right) \tag{4}$$

Given that along the edges of the peak the count statistics tend to be poor for physical reasons, and because the tally will always be less populated at the edges, an average of the counts of the channels (m) located in the Upper edge (U) and the Lower edge (L) of the peak is taken. For this case, taking the average of the four most extreme channels ($m = 4$) was found to provide a good representation of the background.

Regarding uncertainty propagation, the variance for both the background and the gross counts is equal to the variance of the sum of random variables, i.e., the counts per group, that are scaled by the term $n/2m$. The correlation term for the sum between counts per channel is zero since these variables are independent. The physical intuition behind this is that each photon reaching the detector constitutes an independent event. Hence, the variability in the energy of one photon is uncorrelated with the variability in the energy of another photon, since their trajectories and interactions remain independent. The validity of this assumption was confirmed by MC simulations. This leads to the following expression for obtaining the variance of the net peak area and ultimately, since the counts are normalized, to the variance of the efficiency:

$$Var(\mathcal{E}_{MC}) = \sum_{i=L}^{U} \sigma_{MC_i}^2 - \frac{n^2}{4m^2}\left(\sum_{i=L-m}^{U} \sigma_{MC_i}^2 + \sum_{i=U+1}^{U+m} \sigma_{MC_i}^2\right) \tag{5}$$

Where σ_{MC_i} is the standard deviation given by the code for each energy group i.

2.5. Bayesian optimization

Bayesian optimization (BO) uses and iteratively retrains a surrogate of the difference between the calibration measurements and the MC model predictions, i.e., the objective function $f(\theta)$ with θ being the 9D vector of calibration parameters. The considered surrogate model is a Gaussian Process (GP) which is utilized to select "*promising*" points where to run the MC model according to an acquisition policy (AP) that minimizes the distance measured by $f(\theta)$. In this subsection, we introduce a brief formalism of the BO algorithm such that we can later describe how our implementation can

be related to these generic parts of the BO. The pseudo-code of the algorithm is detailed below:

Algorithm 1 Bayesian optimization pseudo-code (minimization)

Requires: $f(\theta)$, $D = \{(\theta_i, y_i)\}$, α
Output: Best solution found θ^*
1. Initialize Gaussian process (surrogate) model with D
while stopping criterion not met:
2. Select next query point $\theta_{\text{next}} \leftarrow \arg\min_{\theta \in -\theta'} \alpha(\theta'; D)$
3. Evaluate $y_{\text{next}} = f(\theta_{\text{next}})$
4. Update $D \leftarrow D \cup \{(\theta_{\text{next}}, y_{\text{next}})\}$
5. Update Gaussian process model
end while
$\theta^* \leftarrow \arg\min_{\theta_i \in D} y_i$

In step 1, The GP model is firstly initialized with an initial dataset D, containing the parameters fed to the objective function $f(\theta)$, and the observed value of the objective function y_i obtained by calculating the simulated FEPEs associated with these initial sets of parameters for all the source-position combinations of the CES experiment. In our case, D is a collection of 25 points, i.e., 25 combinations of parameters plus the associated value of the objective function (25 x 10).

In step 2, once this first GP model is trained, a new candidate θ_{next} (1 x 9) or a batch of candidates q (q x 9), can be selected by optimizing the AP, α. This policy evaluates the GP within the parameter bounds defined for the problem. By doing so, the parameter space is explored in a data-efficient fashion, i.e., the exploration of unknown regions of the objective function and the exploitation of promising regions with a low variance are balanced.

In step 3, we need to obtain y_{next} (q x 1) , i.e., the objective function value(s) at θ_{next} (q x 9), and this is done by running again the MC model for the newly-proposed parameters for the 200 experimental setups (different energies and positions). Running the MC model is the "expensive" step, and we therefore try to minimize the number of MC runs, which means minimizing the number of iterations of the BO since the number of experimental setups is fixed.

In step 4, once the calculations of the batch defined in step 3 are finished, $\{(\theta_{\text{next}}, y_{\text{next}})\}$ (q x 10) is appended to D.

In step 5, now that we more information is available with respect to the objective function landscape, the GP is retrained with the updated D.

The loop defined by steps 2 to 5 continues until a predefined computational budget is consumed.

There are many options available for building the full BO loop. Different initialization methods of D could work with different results depending on which experimental design or sampling technique is being used. The acquisition policy α will eventually depend on the approach followed for BO, maybe the user is interested in manually regulating the trade-off between exploration or exploitation, or perhaps, for a given application it is decided to run parallel evaluations of α ($q > 1$) and then, a scalable method for the AP is preferred. Additionally, different data will be best-fitted by different surrogate models, which implies deciding as well on the parameters of the surrogate. In essence, the BO framework is highly problem-oriented and ideally requires a good knowledge of the problem at hand to choose the best possible implementation. We refer the reader to [8] and to [7] for a deeper and rigorous explanation of BO and GPs respectively.

2.5.1. Objective function

The objective function to be minimized, $f(\theta)$ for all the positions (X, Y) and energies (E) available in the CES experiment, was defined as the average of the L1 norm distance between the measured and simulated FEPEs weighted by the square root of the sum of their variances as expressed by Eq. (6).

$$f\left(x\right) = \frac{1}{n}\sum_{i=1}^{i=n}\left(\frac{|\mathcal{E}_{MC}(E,X,Y)_i - \mathcal{E}_{exp}(E,X,Y)_i|}{\sqrt{\sigma^2_{MC}(E,X,Y)_i + \sigma^2_{exp}(E,X,Y)_i}})\right) \tag{6}$$

This objective function favours fitting those measured efficiencies that have the lowest (both MC and experimental) uncertainties.

2.5.2. Gaussian process surrogate model

The GP method assumes that the joint distribution of the observed values (training data) and the values we want to predict (test data) can be represented as a multivariate normal distribution (MVN). This involves calculating a covariance matrix (the kernel of the GP) using a kernel function $k(\theta, \theta')$, which describes how the values of the objective function change as

the input parameters vary. In other words, the kernel function expresses the similarity between two given points θ and θ'.

In this work, we use the well-known Radial Basis Function (RBF). For a collection of commonly used kernel functions, we refer to [7]. The RBF kernel is given by:

$$k(\theta, \theta') = \sigma^2 exp\left(-\frac{(\theta - \theta')^2}{2l^2}\right) \tag{7}$$

This kernel function has two key hyperparameters: the lengthscale (l), which determines how smooth the function transitions between points, and the output variance (σ), which measures the average spread of the function around its mean.

We chose this kernel through a process called Cross-Validation (CV) [7], which ensures it is the kernel most compatible with our initial dataset. In CV, we iteratively train the model on subsets of the data and validate on the excluded subset, repeating this for each subset. This helps us assess the performance of the model and select the best kernel by observing the standard deviation and average of the misfit between the actual and predicted values for all the repetitions. In this case, 10 subsets, making 10 validations in total.

Training the GP involves optimizing these hyperparameters to best match our data, which is commonly done by maximizing the so-called marginal log-likelihood (MLL) of the GP model [7]. Note that this step is faster than the expensive evaluation made in step 3 of our algorithm.

Once trained (step 5), the GP is used to predict the objective function values for the new sets of parameters. Here the acquisition policy comes into play. The acquisition policy uses the GP's predictions and their uncertainties to determine the next set of parameters to evaluate. Essentially, it decides where in the parameter to sample next by balancing the trade-off between exploring areas with high uncertainty (to learn more about the function) and exploiting areas with low predicted values (which are likely to contain the global minimum). This iterative process continues until the allowed computational budget is exhausted or a given threshold objective function value is reached.

2.5.3. Acquisition policy

In this approach, the update of the dataset is based on batch acquisition ($q = 4$), so four evaluations of $f(\theta)$ are made at each iteration. To choose these promising candidates, Thompson Sampling (TS) [26] is used.

Although many policies can be used to propose next candidates, TS allows for easy parallelization since it scales well with q and is easy to implement, TS is conducted by drawing a sample from the GP, i.e., a realization of the unidentified objective function (a realization of the GP posterior distributions is a function, not a scalar) over a discretized search domain:

$$\alpha_{TS}(\theta; D) \sim p(f|D) \tag{8}$$

TS identifies the optimal (in this case, minimum) value of this randomly drawn sample and evaluates the objective function at that point. This acquisition policy can be viewed as optimizing random acquisition functions, that consists of random draws of the GP posterior [27].

2.5.4. Initial dataset generation

Since the first dataset requires 25 x 200 MC calculations, it is desirable to make those points as informative as possible. For that reason, we resorted to what is known as a space-filling design, which aims to fill the 9D hypervolume as homogeneously as possible for a given number of points. We used an optimized maximin Latin Hypercube Design (LHD) obtained from [28] to create the initial values for D.

It is noticed that the growth of the different dead layers appears to be, to a certain extent, positively correlated for a given detector [2, 4, 29, 30]. Furthermore, a high spread in the marginal distributions of the three dead layer thicknesses is to be expected [2, 4, 29, 30]. To incorporate this behaviour into D, we used a 3D multivariate normal distribution (MVN) with means 0.666, 1.72, and 0.015 and with standard deviations 0.066, 0.17, and 0.01 for the frontal, lateral, and inner dead layer respectively. The correlation for the three parameters was derived from the previous references and set to 0.93 for all three pairs.

Then we resorted to the inverse Rosenblatt [31] transform to convert the uniform [0,1] distribution contained in D to the prescribed MVN. The details of the procedure are as follows.

A vine copula is used for capturing the dependencies between variables in the generated MVN. A vine copula is a flexible and structured way to model complex dependencies among multiple variables using a series of bivariate copulas organized in a hierarchical graphical model. [32]. Next, the Rosenblatt transform converts the normal distributions obtained by the vine copula to a uniform distribution.

Finally, the inverse Rosenblatt transform can be used to convert the initial LHD for the dead layers to a MVN with the prescribed correlations.

Overall, to integrate all the available knowledge for elaborating the distributions for the initial dataset, we proceeded as illustrated by Fig 5.

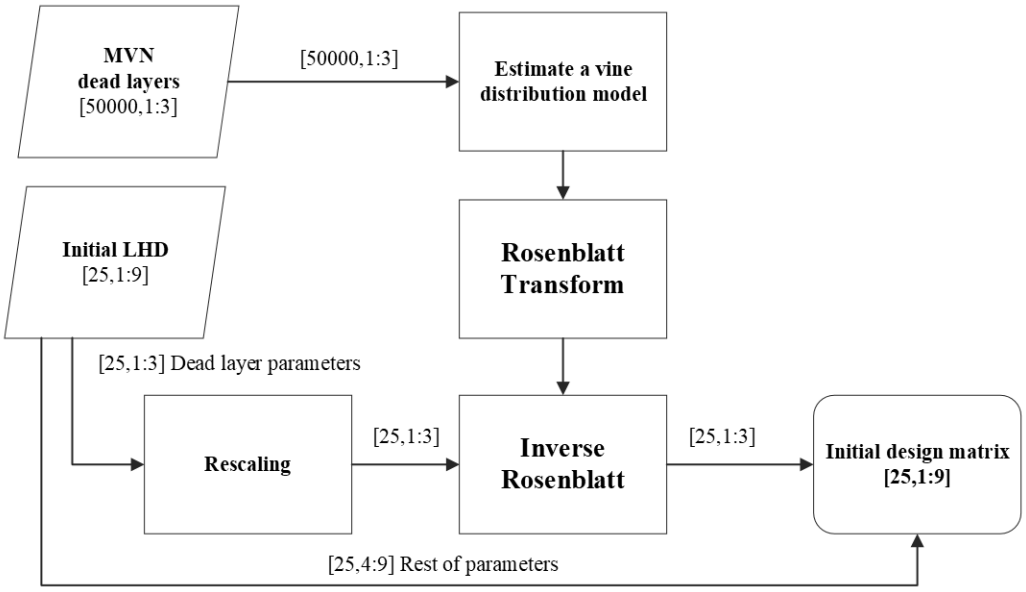

Figure 5: Steps followed to obtain the initial dataset for the surrogate, processes are represented by rectangles, auxiliary datasets are represented by the parallelograms, the final dataset is represented by the rounded corner rectangle. Data size represented between brackets in [rows, initial column:final column] format. Note that for obtaining a robust vine distribution, 50 000 samples were drawn from the MVN.

2.5.5. Implementation

The specific optimization algorithm utilized in this work is known as Trust Region Bayesian Optimization (TuRBO) [27]. BO is very efficient for optimizing hard problems which objective function is expensive, but tends to scale bad for higher-dimensional problems. TuRBO was designed as a local approach for global optimization problems and tries to alleviate the scalability issue of BO by running local GP models on parallel, each model would run q candidates drawn within the trust regions for each iteration, which allows for concurrent evaluation of different query points of the objective function.

The trust regions are volumes defined inside the search space, centered around the best solution found so far. If an iteration is successful (a candidate

is found), the region will double the size in all directions, aiming to explore the space around. However, if the iteration cannot find a better value than the current one, the region will shrink by half the size around the best value found, once the size is minimal (smaller than a size $L_{\min}$, normalized to the GP lengthscales) the optimizer converges and the process finishes.

For this work, only one trust region was used (TurBO-1) and four candidates were proposed for each iteration ($q = 4$). The optimizer for this work was set according to [27] in BoTorch [33], a library for Bayesian optimization built on top of PyTorch [34]. The very same algorithm used on this work is presented for a synthetic case in [35]. Fig. 6 depicts the flow diagram of TuRBO with 1 trust region used in this work.

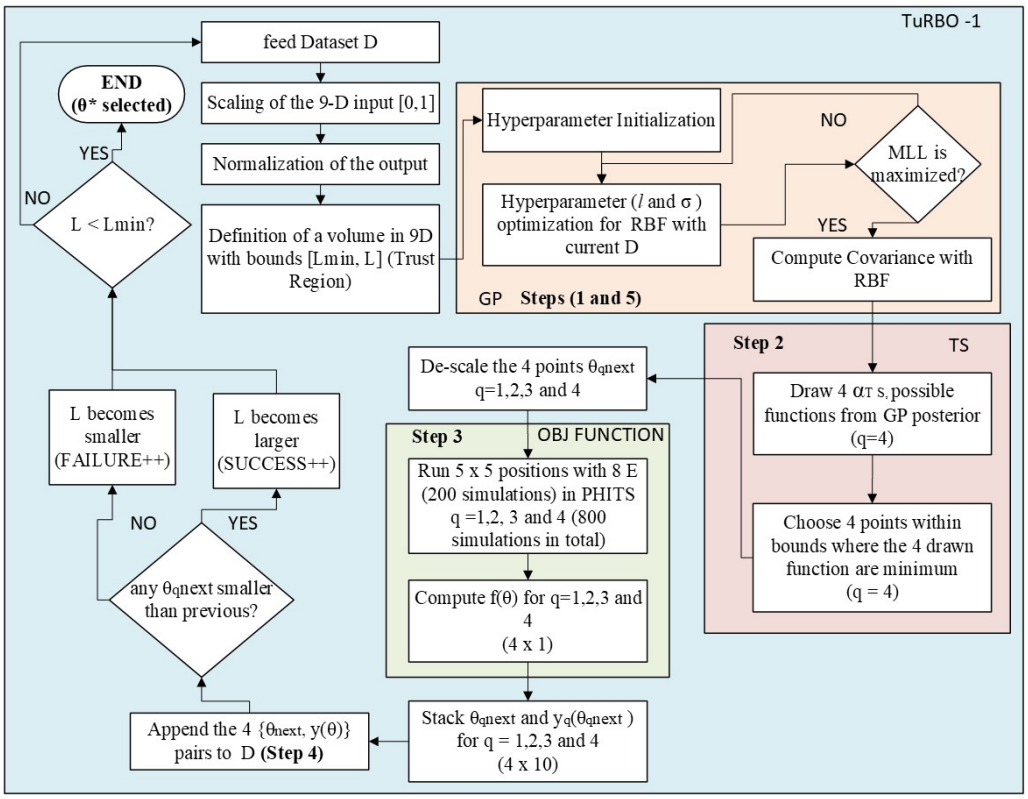

Figure 6: Diagram of the optimization process.

2.5.6. Metrics for validation

In order to evaluate the results, Ratio (R), Zeta-score (ζ_{score}), and Precision Score (P_{score}) were employed as metrics in order to evaluate the deviation of the model, accuracy, and precision of the model, respectively. Said metrics are defined according to Eqs. (9), (10) and (11).

$$R = \frac{\mathcal{E}_{MC}}{\mathcal{E}_{exp}} \tag{9}$$

$$\zeta_{score} = \frac{|\mathcal{E}_{MC} - \mathcal{E}_{exp}|}{\sqrt{\sigma_{MC}^2 + \sigma_{exp}^2}} \tag{10}$$

$$P_{score} = 100\sqrt{\left(\frac{\sigma_{MC}}{\mathcal{E}_{MC}}\right)^2 + \left(\frac{\sigma_{exp}}{\mathcal{E}_{exp}}\right)^2} \tag{11}$$

These metrics are typically employed in the literature for validating radiation detector computational models. Furthermore, ζ_{score} and P_{score} are commonly employed by the IAEA in inter-comparison exercises and proficiency tests [14].

3. Results

3.1. Optimization results

After 16 iterations with four evaluations of the objective function per batch (64 evaluations in total), the optimizer found a set of parameters that lies within the acceptance criteria dictated by the evaluation metrics,as can be found when comparing the CES simulated efficiency for the found parameters to the actual measured efficiency values (Fig. 7). The effective parameters are presented in Table 3.

Table 3: Effective parameters found by the optimizer (iteration 16).

	Parameter	**Bounds**	**Value**
(1)	Frontal DL	[0.60, 1.60]	0.69
(2)	Lateral DL	[0.60, 1.60]	1.40
(3)	Inner DL	[0.01, 0.02]	0.0199
(4)	Dist. Crystal-endcap	[5.30, 7.00]	5.78
(5)	Offset X of detector	[-4, 4]	-3.93
(6)	Offset Y of detector	[-1.50, 1.50]	-0.85
(7)	Coll. Horizontal apert.	[59.00, 61.00]	60.43
(8)	Coll. Vertical apert.	[60.00, 61.00]	60.66
(9)	Slab Angle	[19.00, 20.40]	19.50

As can be observed, there is an evident offset in the detector position with respect to the lead shielding center in both horizontal (5) and vertical (6) coordinates. Additionally, the distance from the Crystal to the endcap (4) found is similar to the measured via X-Ray imaging (Fig. 1b).

The asymmetry found in the positioning corresponds to the effect of the efficiency values noticeable in Fig. 7, specially in the lateral source positions (X=-8 cm and X= 8 cm). As for the general response of the detector for each position, it can be noted how the efficiency exponentially decreases over energy after reaching its maximum at 120 keV, as expected according to the working principle of the detector. Furthermore, the attenuation that the collimator exerts on the efficiency is clear, especially in the vertical direction when the source is placed 8 cm away from the center of the detector (Y=-8 cm and Y= 8 cm). Regarding the uncertainty and reliability of the accrued measurements, it is worth noting that the experimental uncertainty σ_{exp} (k = 1) always covers the FEPEs obtained via MC with the exception of the ^{241}Am peak in the position (-8,8).

3.2. Validation results

This section presents the VE1 and VE2 validation experiments. First, the validation of the detector internals was performed by computing the FEPEs for the positions in VE1 (no collimator). The comparison of the corresponding measured and calculated FEPEs is shown in Fig. 8. The validation of the collimator parameters, relying on VE2, is then shown in Fig. 9 and in Fig. 10 for the collimator opened at 40 mm and 50 mm, respectively.

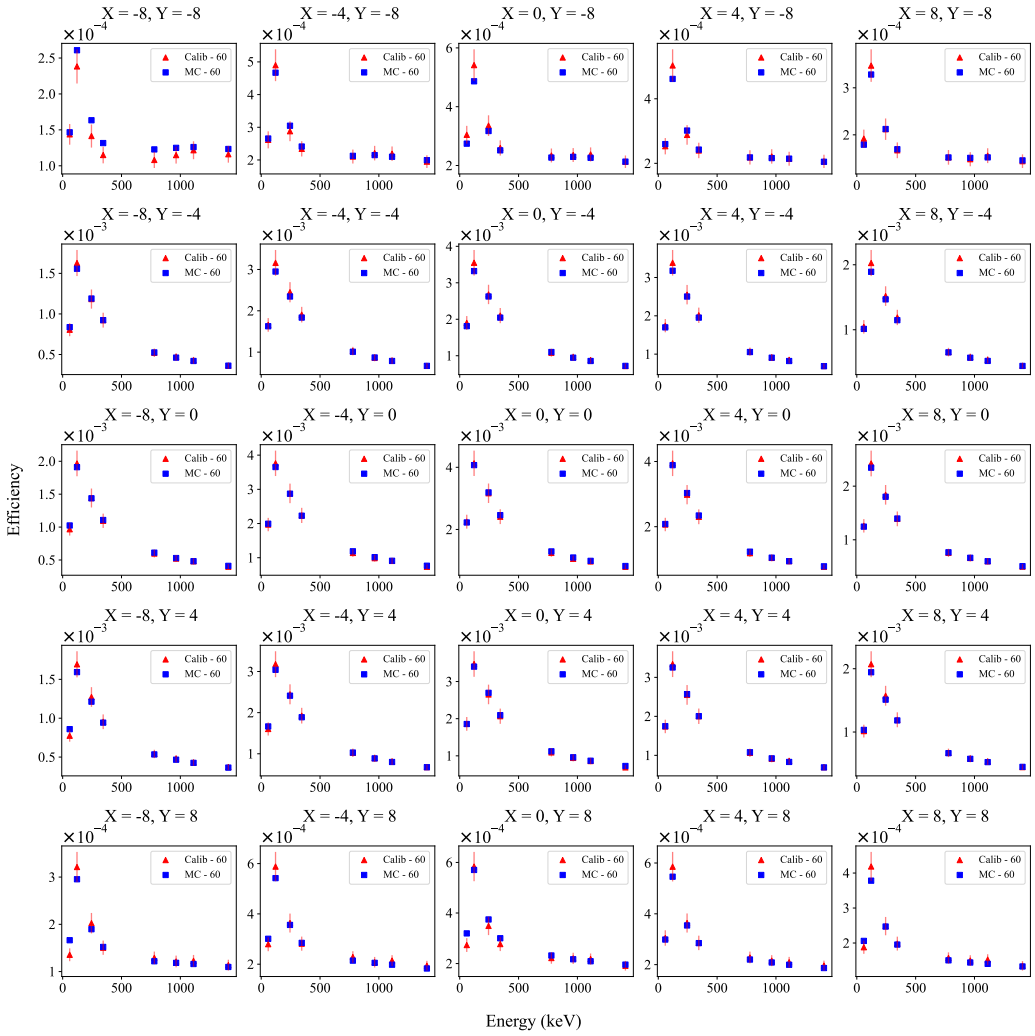

Figure 7: FEPE values for the 25 positions of CES for americium and europium peaks, collimator at 60 mm. X and Y indicate the position of the source in cm. In blue the simulated FEPE, and in red, the measured FEPE. The MC error is not depicted here for being small.

Simulations from the calibrated model show a good agreement with VE1 measurements for all the positions. All the simulated FEPE indeed lie within the uncertainty of the measured FEPEs.

Basically, for the higher end of the considered energy range, the response of an uncollimated detector (VE1 experiment, Fig. 8) is much less sensitive to

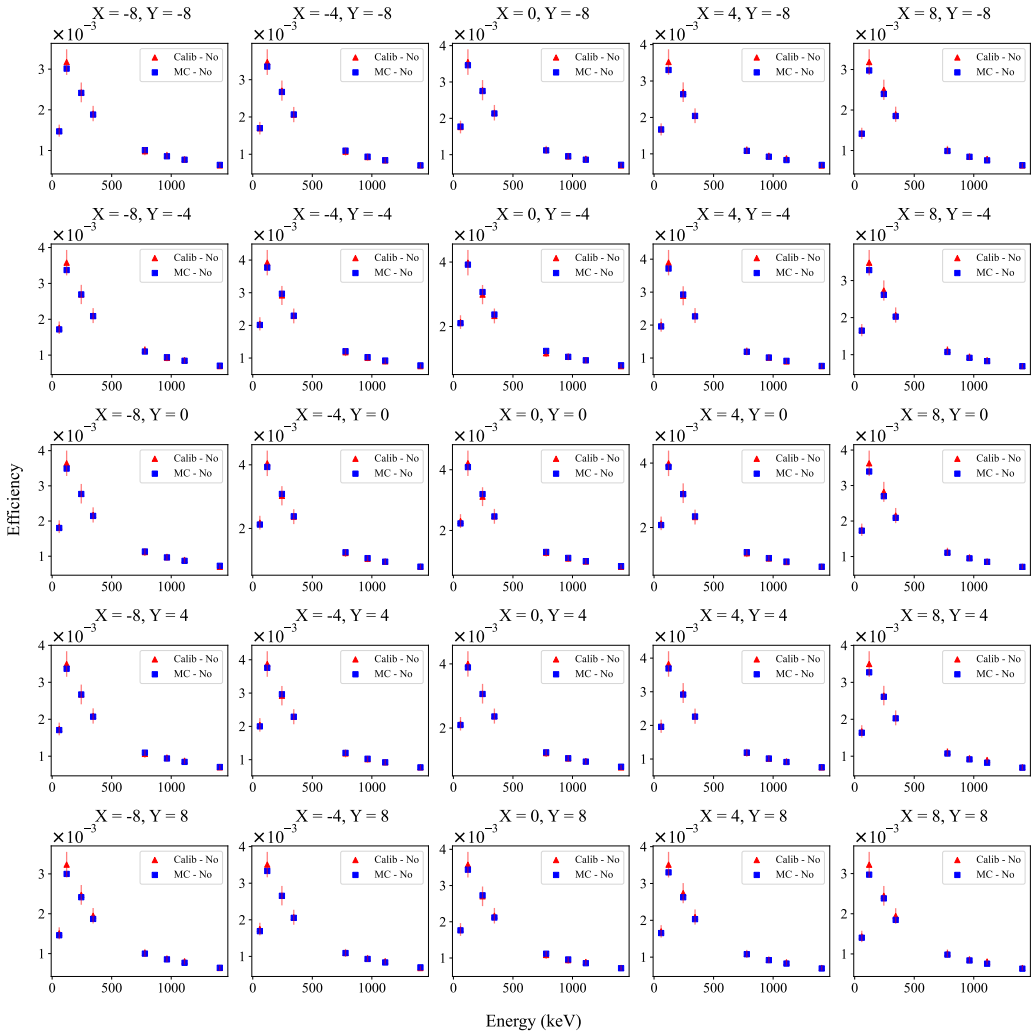

Figure 8: FEPE values for the 25 positions of VE1 for americium and europium peaks, No collimator attached. X and Y indicate the position of the source in cm. In blue the simulated FEPE, and in red, the measured FEPE. The MC error is not depicted here for being small.

the variations in source positions than the response of a collimated detector (VE2 experiment, Figures 9 and 10).

Regarding VE2, an overall good agreement between the simulated and the experimental data, except for the positions (8,-8) and (8,8) cm when the

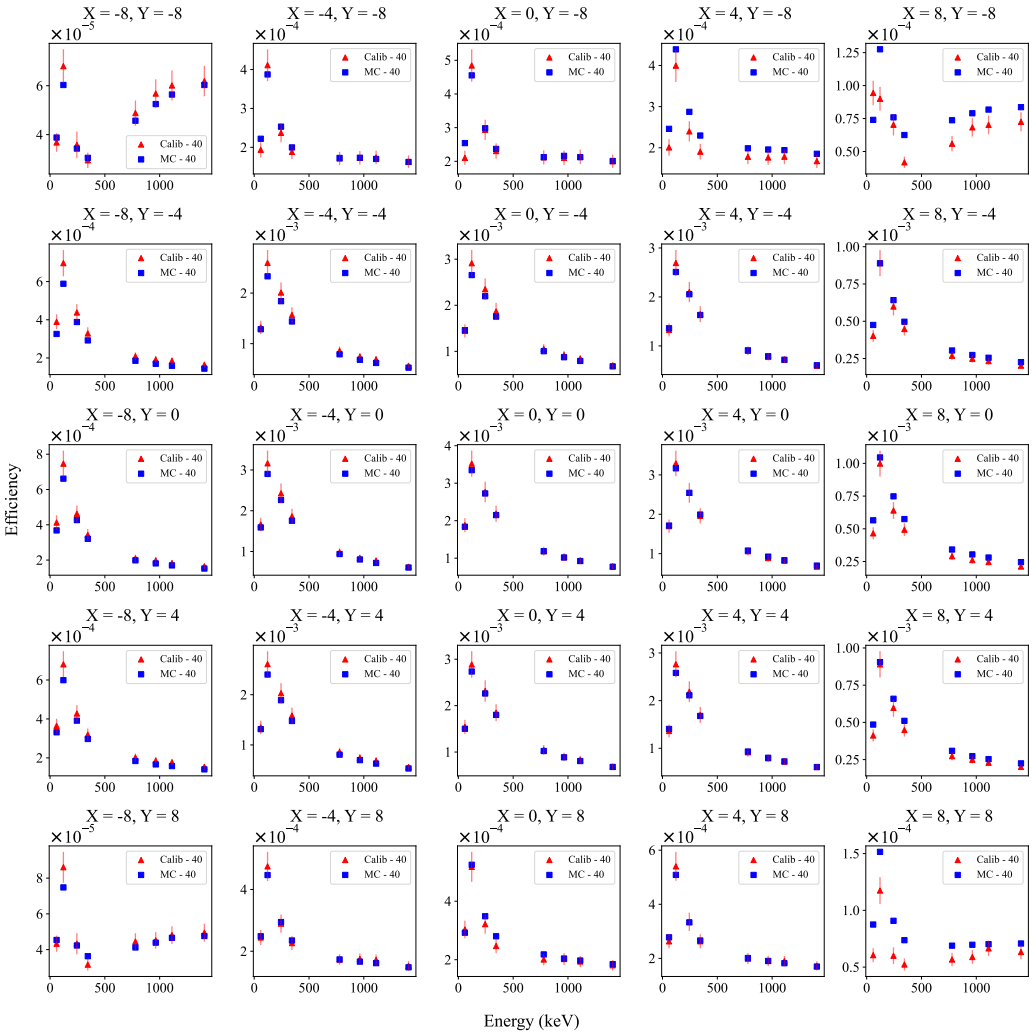

Figure 9: FEPE values for the 25 positions of VE2 for americium and europium peaks, collimator opened at 40 mm. X and Y indicate the position of the source in cm. In blue the simulated FEPE, and in red, the measured FEPE. The MC error is not depicted here for being small.

collimator aperture is 40 mm (Fig. 9).

In the case of the collimator opened at 50 mm (Fig. 10), it can be noticed a better agreement between the simulated and the measured FEPEs for the position (8,-8) and in general, a better fit for every source positions,

is observed.

Nonetheless, we would like to stress that several measured FEPE values belonging to the (8,-8), (8,8) and (-8,8) cm positions were measured from low intensity peaks (relative low count rates with respect to other peaks measured in the same arrangement and/or with respect to other peaks belonging to the same spectrum) and hence, with a noisy background.

This could cause errors when calculating both background and peak areas, since the manufacturer's software tries to fit a Gaussian distribution to the region of interest (ROI) of the peak.

Given the used measurement time and the measured total counts, the associated measured FEPE values were deemed to be statistically unreliable. For positions 8 cm away from the detector windows, measured data corresponding to net count rates lower than 20 cps where therefore excluded from the optimization.

We now turn attention to the evaluation metrics introduced in section 2.7. The first one is ζ_{score}, shown in Fig. 11 for each collimator aperture and VE1 (no collimator).

Drawn in red, is the limit of 2.58, which is considered to be the critical value for a normal distribution with a confidence level of 99 % [14].

For VE1 and CES, all 200 points of the arrangements are below the critical limit and for CES, only some outliers have values greater than 1, values that are from FEPEs measured in the most peripheral positions (8 cm away from the detector window).

Nonetheless, in VE2, there are some outliers greater than 2.58, when the collimator is at 50 mm, 98.5 % of the points are below the 2.58 limit, and only 3 outliers are, out of limits. When the collimator is closed up to 40 mm, the number of outliers exceeding critical limits increase, but still 97 % of the points are within acceptance criteria.

These outliers are the FEPEs measured at positions (8,8) and (8,-8) for the collimator opened at 40 and 50 mm. Positions that were known to be noisy, as previously stated. Additionally, note that there is a clear increase in the difference between measured and simulated FEPEs when the collimator is present (VE2 40 mm and 50 mm in Fig. 11). The same situation is seen for the ratio criterion (Fig. 12).

Here too, outliers are associated with the (8,8), (-8,8) and (-8,-8) source positions. Even though 71.5% of the points are within 10% of deviation (marked in red) and 87% lie with 15 % of deviation , there are also points that reach more than 20 % of deviation among the values observed for VE1.

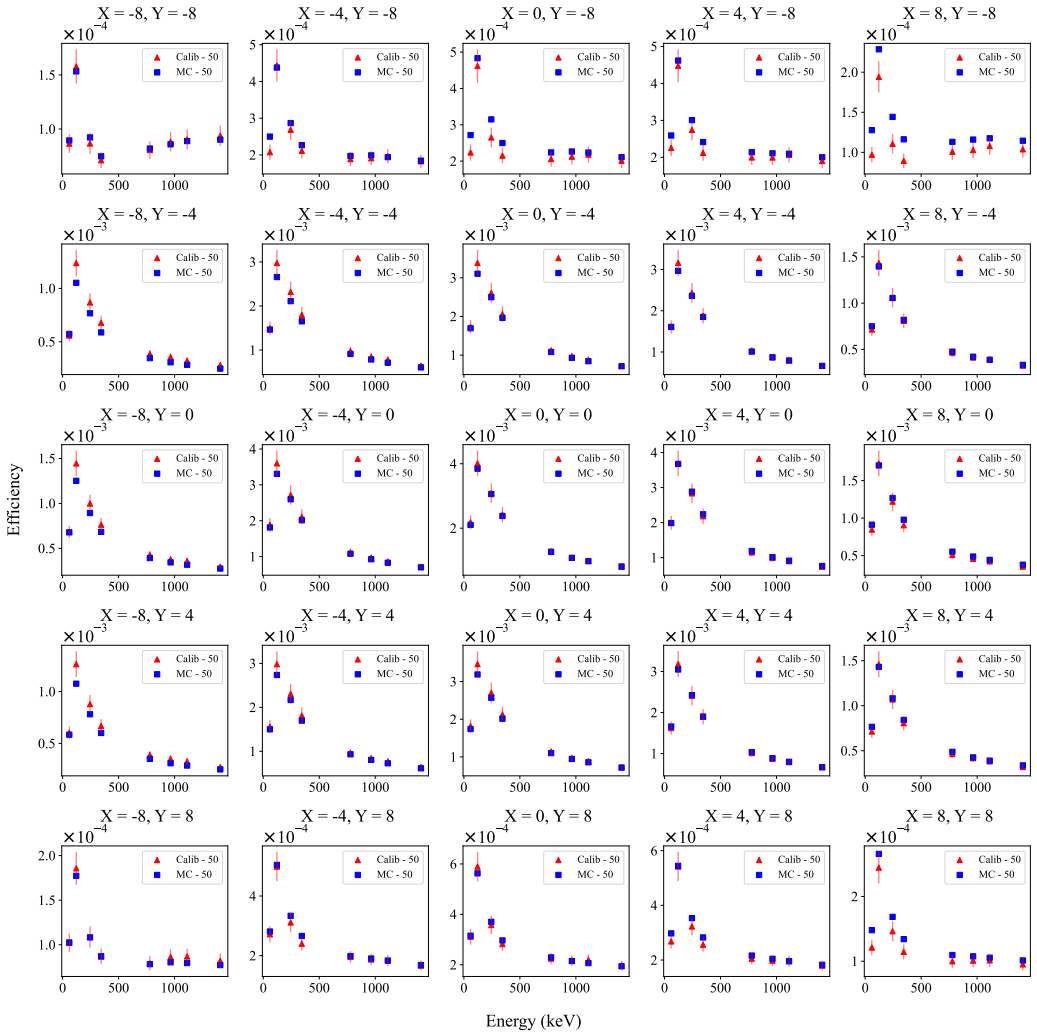

Figure 10: FEPE values for the 25 positions of VE2 for americium and europium peaks, collimator opened at 50 mm. X and Y indicate the position of the source in cm. In blue the simulated FEPE, and in red, the measured FEPE. The MC error is not depicted here for being small.

These outlier values again correspond to the peripheral positions measured 8 cm away from the detector window. Additionally, it is seen that the average ratio for each experiment lies exactly on 1.0, which means that there is no bias in the simulated FEPEs.

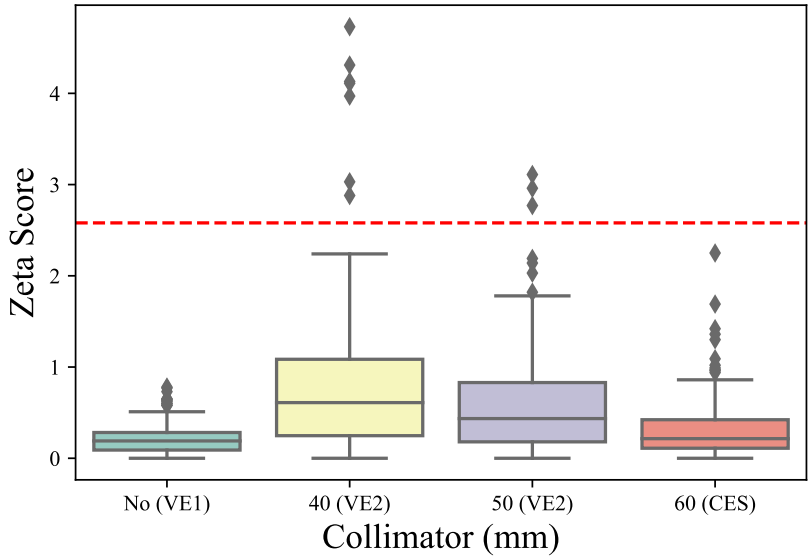

Figure 11: ζ_{score} box plot for each experimental arrangement.

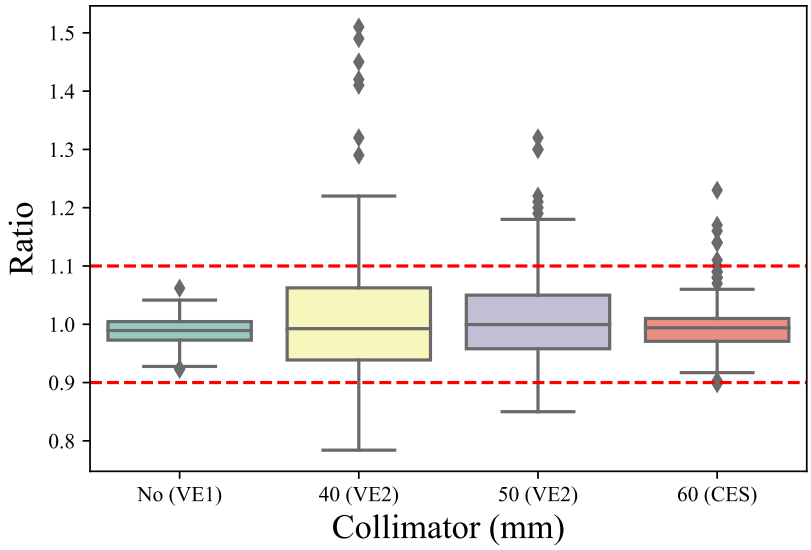

Figure 12: Ratio box plot for each experimental arrangement.

Finally, the Precision score, P_{score}, is presented for all the experiments in Fig. 13.

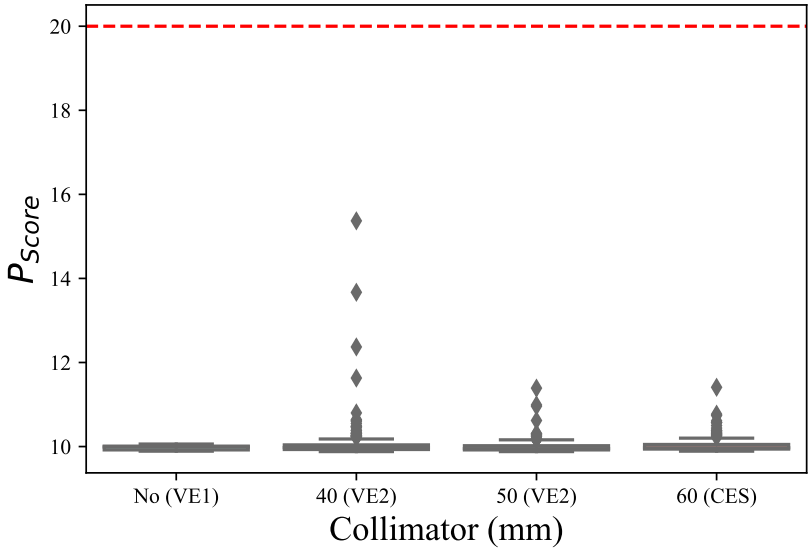

Figure 13: P_{score} box plot for each experimental arrangement.

The values of P_{score} are always way below the agreed critical limit of 20 [13], marked in red. Additionally, it is found that the P_{score} values are well centered around 10% since the source position error is dominating the error in the MC calculations (see expression 11).

4. Discussion

4.1. Validity of the model

According to our results, it can be assumed that the calibrated detector model is valid for predicting FEPEs in SGS scenarios where it is necessary to simulate SGS use cases taking into account the position of the source for the 50 to 1400 keV energy range.

With respect to the VE2 validation tests, which involve the collimated detector with two apertures not used for calibration, the calibrated performs generally well although not surprisingly somewhat less well than for the validation without collimator (VE1).

However, it is important to note that the variation in the measured FEPEs between these most peripheral source positions and the center position (source in front of the detector window) can be up to two orders of

magnitude. We argue that deriving a calibrated model with such a flexibility is a huge challenge, if at all possible. As stated above, we consider our calibrated model to be well validated.

4.2. Validity of the found parameters

The parameters can be considered valid if they are considered effective parameters, i.e. they have values that allow the computational model to perform in a homologous way to the real equipment even if they are not the real values.

As far as the internal detectors (1 to 4 in Table 3) are concerned, they appear to make sense according to the good results obtained in VE1, although obviously the found values can only be compared with those in the literature.

On the one hand, it is confirmed that the lateral dead layer is thicker, slightly more than twice as large as the front layer. On the other hand, the crystal-endcap distance is in line with what was observed via X-rays.

Additionally, it is confirmed that the internal dead layer (electrode side) hardly affects the simulated FEPE values. This was verified by checking that no significant variation of the FEPEs was observed for these source-position arrangements for any value of the internal dead layer thickness ranging from 0.005 to 0.04 mm when running the optimized model (the bounds for this parameter were 0.01 and 0.02 mm).

As for the position of the detector (parameters 4 to 6), it is observed that the offset in X determined by the optimisation is perhaps (taking into account that we cannot check the centering inside the detector casing) somewhat exaggerated, however, this value works to compensate for the asymmetry found in the FEPE values in the horizontal direction. Finally, the derived geometrical parameters of the collimator, agree well with those measured on the real equipment.

4.3. Optimization methodology

Firstly, it has been observed how BO can find the studied parameters simultaneously with a reduced number of objective function evaluations.

The objective function used has been proven to work correctly within the optimization framework. The purpose of this objective function was to take into account the noise present in real measurements, relying less on those with worse statistics. Traditional Root Mean Squared Error (RMSE) proved to be convenient too, but more evaluations of the objective function were required to reach acceptable results.

The fast convergence of TuRBO used in this case surely depends on the initial distributions used in the design matrix required to produced the starting dataset. As has been verified, it is effective to use a MVN to model the relationship of the dead layers, assuming that the thickness of these is positively correlated. On the other hand, it seems that the chosen parameters are representative enough of the problem, being sufficient for calibrating the spatial and spectral response of the detector.

Lastly, we would like to stress that the optimization process, although informed and efficient, remains computationally intensive due to the number of MC simulations necessary for the evaluation of the objective function. Since the peaks were separatedly calculated, 8 calculations were required for each combination of detector - source positions. In total, for each evaluation of the objective function, 200 calculations were needed, requiring 40 cores each to be completed in less than 20 minutes.

For this reason, it would be interesting not to simulate points that are lowly informative for modeling the collimator and the detector simultaneously.

One option to assess the information content of a parameter set before actually simulating it with the computationally-demanding MC code would be to create a computationally-efficient surrogate model of the MC model of the detector directly (rather than that of the misfit between MC-simulated and measured counts). This surrogate model (or metamodel or emulator), which could be a GP or another nonlinear regressor, would then be able to predict the FEPE based on the position, the energy of the source, and other relevant parameters of the measurement setup. If successfully trained, such a computationally cheap digital twin could be combined with Bayesian Optimal Experimental Design techniques to obtain, on the one hand, the most informative points where to position the sources in a real-world experiment, and on the other hand, the geometric parameters that most affect the FEPE. This will be explored in future work.

In the same line of work, being able to successfully train an efficient digital twin of the optimized MC model taking into account all the parameters studied here, will allow us in the future to optimize the measurement setups for a given waste package, for example, obtaining optimal sampling time assessed via Minimum Detectable Activity (MDA), or providing optimal distances or collimator apertures for a given waste package.

5. Conclusion

It has been demonstrated that the methodology used here based on Bayesian optimization, allows for the identification of effective parameters to validate complex computational models of SGS equipment taking into account all the relevant parameters that affect the detector response, whether collimated or uncollimated.

The model calibrated following this methodology performs well when predicting the spatial and spectral response of the real detector, which has been verified for different collimator configurations.

Acknowledgements

The authors would like to thank Benjamin Hennebert, from Syscade for taking the measurements.

This work was funded by the Recovery and Resilience Facility (RRF) of the European Union under the NextGenerationEU program as part of the ANUBIS project [Advancing NUclear dismantling in Belgium through Improving Sustainability] and by the Flemish Government under the 'Onderzoeksprogramma Artificiële Intelligentie (AI) Vlaanderen'. We gratefully acknowledge the financial support and the opportunities provided by this initiative.

Declaration of competing interest

The authors declare that they have no known competing financial interests or personal relationships that influenced the work reported in this paper.

CRediT author statement

Victor J. Casas-Molina: Conceptualization, Methodology, Software, Validation, Formal Analysis, Investigation, Writing - Original Draft, Writing - Review & Editing. **Eric Laloy:** Supervision, Project administration, Methodology, Resources, Writing - Review & Editing. **Bart Rogiers:** Supervision, Project administration, Methodology, Writing - Review & Editing **Ivo Couckuyt:** Supervision, Project administration, Methodology, Resources, Writing - Review & Editing. **Tom Dhaene:** Supervision, Project administration.

References

[1] M. M. Hasan, T. Vidmar, J. Rutten, L. Verheyen, J. Camps, and M. Huysmans, "Optimization and validation of a LaBr3(Ce) detector model for use in Monte Carlo simulations," *Applied Radiation and Isotopes*, vol. 174, p. 109790, Aug. 2021.

[2] L. T. N. Trang, H. D. Chuong, and T. T. Thanh, "Optimization of p-type HPGe detector model using Monte Carlo simulation," *Journal of Radioanalytical and Nuclear Chemistry*, vol. 327, pp. 287–297, Jan. 2021.

[3] H. D. Chuong, T. T. Thanh, L. T. Ngoc Trang, V. H. Nguyen, and C. V. Tao, "Estimating thickness of the inner dead-layer of n-type HPGe detector," *Applied Radiation and Isotopes*, vol. 116, pp. 174–177, Oct. 2016.

[4] A. Arectout, H. Boukhal, E. Chham, E. Chakir, F. Piñero García, M. Azahra, H. El Yaakoubi, K. Laazouzi, T. El Ghalbzouri, and M. Assalmi, "Assessment of dead layers thickness of an HPGe detector after an extended operating period using response surface methodology and Box–Behnken design," *Radiation Detection Technology and Methods*, vol. 7, Oct. 2023.

[5] H. Suxia, L. Jijun, L. Rusong, and W. Yongcang, "The collimator shape design of segmented gamma-ray scanning for radioactive waste," *Annals of Nuclear Energy*, vol. 135, p. 106965, Jan. 2020.

[6] M. Malu, G. Dasarathy, and A. Spanias, "Bayesian optimization in high-dimensional spaces: A brief survey," in *2021 12th International Conference on Information, Intelligence, Systems & Applications (IISA)*, pp. 1–8, 2021.

[7] C. E. Rasmussen, "Gaussian Processes in Machine Learning," in *Advanced Lectures on Machine Learning: ML Summer Schools 2003, Canberra, Australia, February 2 - 14, 2003, Tübingen, Germany, August 4 - 16, 2003, Revised Lectures* (O. Bousquet, U. von Luxburg, and G. Rätsch, eds.), pp. 63–71, Berlin, Heidelberg: Springer Berlin Heidelberg, 2004.

[8] R. Garnett, *Bayesian Optimization*. Cambridge University Press, 2023.

[9] A. Gelman, J. B. Carlin, H. S. Stern, and D. B. Rubin, *Bayesian Data Analysis*. Chapman and Hall/CRC, 2nd ed. ed., 2004.

[10] M. Rotty, T. Delvigne, and B. Hennebert, "Combining X-Ray Inspection and Radiologic Characterization for a Better Evaluation of Total Radioactivity Content in Nuclear Wastes," Feb. 2023. SYSCADE presentation in WMS 2023.

[11] J. Ródenas, A. Pascual, I. Zarza, V. Serradell, J. Ortiz, and L. Ballesteros, "Analysis of the influence of germanium dead layer on detector calibration simulation for environmental radioactive samples using the Monte Carlo method," *Nuclear Instruments and Methods in Physics Research Section A: Accelerators, Spectrometers, Detectors and Associated Equipment*, vol. 496, pp. 390–399, Jan. 2003.

[12] N. Q. Huy, D. Q. Binh, and V. X. An, "Study on the increase of inactive germanium layer in a high-purity germanium detector after a long time operation applying MCNP code," *Nuclear Instruments and Methods in Physics Research Section A: Accelerators, Spectrometers, Detectors and Associated Equipment*, vol. 573, pp. 384–388, Apr. 2007.

[13] J. G. Guerra, J. G. Rubiano, G. Winter, A. G. Guerra, H. Alonso, M. A. Arnedo, A. Tejera, P. Martel, and J. P. Bolivar, "Computational characterization of HPGe detectors usable for a wide variety of source geometries by using Monte Carlo simulation and a multi-objective evolutionary algorithm," *Nuclear Instruments and Methods in Physics Research Section A: Accelerators, Spectrometers, Detectors and Associated Equipment*, vol. 858, pp. 113–122, June 2017.

[14] J. G. Guerra, J. G. Rubiano, G. Winter, A. G. Guerra, H. Alonso, M. A. Arnedo, A. Tejera, P. Martel, and J. P. Bolivar, "Modeling of a HPGe well detector using PENELOPE for the calculation of full energy peak efficiencies for environmental samples," *Nuclear Instruments and Methods in Physics Research Section A: Accelerators, Spectrometers, Detectors and Associated Equipment*, vol. 908, pp. 206–214, Nov. 2018.

[15] S. Kaya, N. Celik, and T. Bayram, "Effect of front, lateral and back dead layer thicknesses of a hpge detector on full energy peak efficiency,"

Nuclear Instruments and Methods in Physics Research Section A: Accelerators, Spectrometers, Detectors and Associated Equipment, vol. 1029, p. 166401, Apr. 2022.

[16] M. J. Vargas, A. F. Timón, N. C. Díaz, and D. P. Sánchez, "Influence of the geometrical characteristics of an HpGe detector on its efficiency," *Journal of Radioanalytical and Nuclear Chemistry*, vol. 253, pp. 439–443, Sept. 2002.

[17] M. Ješkovský, A. Javorník, R. Breier, J. Slučiak, and P. P. Povinec, "Experimental and Monte Carlo determination of HPGe detector efficiency," *Journal of Radioanalytical and Nuclear Chemistry*, vol. 322, pp. 1863–1869, Dec. 2019.

[18] A. Arectout, H. Boukhal, E. Chakir, E. Chham, M. A. Ferro-García, F. Piñero-García, M. Azahra, M. Makhloul, M. Azougagh, H. El Yaakoubi, I. Zidouh, and V. M. Expósito-Suárez, "Optimization of the n-type HPGe detector parameters using the "design of experiments" technique," *Radiation Physics and Chemistry*, vol. 189, p. 109733, Dec. 2021.

[19] T. Vidmar, "EFFTRAN—A Monte Carlo efficiency transfer code for gamma-ray spectrometry," *Nuclear Instruments and Methods in Physics Research Section A: Accelerators, Spectrometers, Detectors and Associated Equipment*, vol. 550, pp. 603–608, Sept. 2005.

[20] M.-M. Be, V. Chiste, C. Dulieu, E. Browne, C. Baglin, V. Chechev, N. Kuzmenko, R. L. Helmer, F. Kondev, and T. D. Macmahon, *Table of radionuclides*, vol. 1,2,3. Bureau International des Poids et Mesures, 2006.

[21] T. Sato, Y. Iwamoto, S. Hashimoto, T. Ogawa, T. Furuta, S.-i. Abe, T. Kai, P.-E. Tsai, N. Matsuda, H. Iwase, N. Shigyo, L. Sihver, and K. Niita, "Features of Particle and Heavy Ion Transport code System (PHITS) version 3.02," *Journal of Nuclear Science and Technology*, vol. 55, pp. 684–690, June 2018. Publisher: Taylor & Francis _eprint: https://doi.org/10.1080/00223131.2017.1419890.

[22] H. Hirayama, Y. Namito, A. F. Bielajew, S. J. Wilderman, and W. R. Nelson, "The EGS5 code system," tech. rep., Japan, 2005. KEK–2005-8.

[23] R. Mcconn, C. Gesh, R. Pagh, R. A. Rucker, and R. Williams, "Compendium of Material Composition Data for Radiation Transport Modeling," Jan. 2011.

[24] J. Boson, G. Ågren, and L. Johansson, "A detailed investigation of HPGe detector response for improved Monte Carlo efficiency calculations," *Nuclear Instruments and Methods in Physics Research Section A: Accelerators, Spectrometers, Detectors and Associated Equipment*, vol. 587, pp. 304–314, Mar. 2008.

[25] G. Gilmore, "Statistics of Counting," in *Practical Gamma-Ray Spectrometry*, pp. 101–129, John Wiley & Sons, Ltd, Apr. 2008.

[26] W. R. Thompson, "On the likelihood that one unknown probability exceeds another in view of the evidence of two samples," *Biometrika*, vol. 25, no. 3/4, pp. 285–294, 1933.

[27] D. Eriksson, M. Pearce, J. R. Gardner, R. Turner, and M. Poloczek, "Scalable global optimization via local bayesian optimization," *CoRR*, vol. abs/1910.01739, 2019.

[28] A. Grosso, A. R. M. J. U. Jamali, and M. Locatelli, "Finding maximin latin hypercube designs by Iterated Local Search heuristics," *European Journal of Operational Research*, vol. 197, pp. 541–547, Sept. 2009.

[29] M. H. Bölükdemir, E. Uyar, G. Aksoy, H. Ünlü, H. Dikmen, and M. Özgür, "Investigation of shape effects and dead layer thicknesses of a coaxial HPGe crystal on detector efficiency by using PHITS Monte Carlo simulation," *Radiation Physics and Chemistry*, vol. 189, p. 109746, Dec. 2021.

[30] K. H. Satti, M. T. Siddique, M. Dilband, S. U. Rehman, S. Mansoor, and A. H. Malik, "A novel method to estimate the dead layer of HPGe detector for Monte Carlo FEPE computation," *Applied Radiation and Isotopes*, vol. 202, p. 111067, Dec. 2023.

[31] M. Rosenblatt, "Remarks on a Multivariate Transformation," *The Annals of Mathematical Statistics*, vol. 23, no. 3, pp. 470–472, 1952. Publisher: Institute of Mathematical Statistics.

[32] C. Czado, *Analyzing Dependent Data with Vine Copulas: A Practical Guide With R*, vol. 222 of *Lecture Notes in Statistics*. Cham: Springer International Publishing, 2019.

[33] M. Balandat, B. Karrer, D. R. Jiang, S. Daulton, B. Letham, A. G. Wilson, and E. Bakshy, "BoTorch: A Framework for Efficient Monte-Carlo Bayesian Optimization," in *Advances in Neural Information Processing Systems 33*, 2020.

[34] A. Paszke, S. Gross, F. Massa, A. Lerer, J. Bradbury, G. Chanan, T. Killeen, Z. Lin, N. Gimelshein, L. Antiga, A. Desmaison, A. Kopf, E. Yang, Z. DeVito, M. Raison, A. Tejani, S. Chilamkurthy, B. Steiner, L. Fang, J. Bai, and S. Chintala, "Pytorch: An imperative style, high-performance deep learning library," in *Advances in Neural Information Processing Systems 32*, pp. 8024–8035, Curran Associates, Inc., 2019.

[35] "BoTorch · Bayesian Optimization in PyTorch - BO with TuRBO-1 and TS/qEI." https://botorch.org/tutorials/turbo_1. Accessed: 2024-07-02.